MALAYSIAN JOURNAL OF MICROSCOPY

Journal homepage: https://malaysianjournalofmicroscopy.org

RESEARCH ARTICLE

INFLUENCE OF CHROMIUM SUBSTITUTION ON THE STRUCTURAL AND ELECTRICAL PROPERTIES OF MAGNESIUM TITANIUM PHOSPHATE CERAMIC ELECTROLYTES PREPARED VIA SOL-GEL METHOD

Muhammad Habib Shehri[1], Nuramani Najihah Ibrahim[1], Noriah Abdul Wahab[1], Nur Amalina Mustaffa[1,*], Siti Rudhziah Che Balian[2], Nurul Akmaliah Dzulkurnain[3]

[1]Faculty of Applied Sciences, Universiti Teknologi MARA, 40450 Shah Alam Selangor, Malaysia.
[2]Centre of Foundation Studies, Universiti Teknologi MARA, Cawangan Selangor, Kampus Dengkil, 43900 Dengkil, Selangor, Malaysia.
[3]International Battery Center (IBC) Sdn. Bhd, HEBATT, Lot-G4, HIVE 8 Taman Teknologi, MRANTI, Bukit Jalil, 57000 Kuala Lumpur, Malaysia.

Abstract. Magnesium-based electrolytes have gained significant popularity recently among researchers as an environmentally friendly alternative to lithium electrolytes. In this study, Magnesium Titanium Phosphate with the substitution of Chromium, $Mg_{0.5+\frac{x}{2}}Cr_xTi_{2-x}(PO_4)_3$ceramic electrolytes were synthesized using the sol-gel method, with various x values. The impact of these x values of 0.1, 0.3, 0.5, 0.7, and 0.9 on the structural and electrical properties of the $Mg_{0.5+\frac{x}{2}}Cr_xTi_{2-x}(PO_4)_3$ samples was then investigated. X-ray Diffraction analysis revealed that the samples exhibited a hexagonal-shaped NASICON-type structure with R3c symmetry and some minor unidentified impurities across x values of 0.1, 0.3, 0.5, 0.7, and 0.9. Additionally, Fourier Transform Infrared analysis showed that the dominant vibrations in the samples came from the PO_4 tetrahedra. Microstructural analysis shows that increasing the Chromium content from 0.1 to 0.9 progressively refines the grain structure, resulting in smaller and more homogeneous grains. The electrical properties were then evaluated using Electrochemical Impedance Spectroscopy, revealing that the highest bulk conductivity of the samples occurred at x = 0.9 (8.97×10^{-8} S.cm^{-1}), while the highest grain boundary conductivity of the samples was observed at x = 0.1 (4.66×10^{-9} S.cm^{-1}). The greatest total conductivity of the samples was achieved at x = 0.1 with a value of 4.42×10^{-9} S.cm^{-1}. Overall, the findings suggest that varying the x value significantly influences the structural and electrical properties of the $Mg_{0.5+\frac{x}{2}}Cr_xTi_{2-x}(PO_4)_3$ceramic electrolytes.

Keywords: Magnesium, ceramic electrolytes, NASICON, sol-gel, chromium-doped.

Article Info

Received 2 May 2025
Accepted 30 October 2025
Published 4 December 2025

***Corresponding author: nuramalina@uitm.edu.my**

ISSN: 1823-7010, eISSN: 2600-7444

1. INTRODUCTION

As batteries age, their performance typically declines, affecting factors such as available capacity, usable energy, and effective power. Rechargeable batteries are a significant energy source for many electronic devices [1]. Over the past few decades, battery technology has advanced, leading to the development of electrical energy storage (EES) devices that are integrated with grids and electric vehicles [2]. Recently, substantial research has focused on improving the electrochemical performance of lithium-ion batteries, which offer advantages such as high voltage, power, energy density, and long cycle life. However, safety concerns exist, as issues like overcharging, overheating, or short-circuiting can lead to fires or explosions [3].

There has been a growing interest in magnesium batteries as a potential alternative to lithium batteries due to their lower raw material costs and reduced hazards [4]. Magnesium offers several benefits, including greater chemical stability compared to lithium and sodium [2-4]. Magnesium batteries are considered promising for modern energy storage systems, as they operate at voltages between 1.0 V - 1.2 V, have an energy density of around 80 $Wh.kg^{-1}$, and can endure up to 1000 discharge cycles across a wide temperature range. Electrochemically, magnesium possesses a high theoretical specific charge capacity (2205 $A{\cdot}h\ kg^{-1}$) and energy density (3.8 $A{\cdot}h\ cm^{-3}$), making it a strong candidate for battery applications [5,6].

To address the limitations of lithium-ion batteries, a solid electrolyte with high ionic conductivity, low electronic conductivity, and good electrochemical stability is required. NASICON (Sodium Superionic Conductor)-type solid electrolytes are considered a promising alternative for commercial batteries [7]. The general formula for NASICON, $A_xB_2(PO_4)_3$, typically contains mono- or divalent cations at A, while B is often occupied by divalent, trivalent, or tetravalent cations. The structure consists of a covalent network of $[B_2P_3O_{12}]$ formed by PO_4 tetrahedra sharing corners with BO_6 octahedra, creating interconnected 3D channels for ion movement [8].

Additionally, Makino et al. [9] successfully synthesized magnesium electrodes using the NASICON structure, including compounds like $Mg_{0.5}Ti_2(PO_4)_3$, $Mg_{0.5+y}(Fe_yTi_{1-y})_2(PO_4)_3$, and $Mg_{0.5+y}(Cr_yTi_{1-y})_2(PO_4)_3$. Li^+ ions replace Mg^{2+} in the NASICON structure. The ionic radius difference between Li^+ (0.69 Å) and Mg^{2+} (0.65 Å) remains within 15%, ensuring that the solubility limit is not exceeded [4]. The substitution of Zr^{4+} ions with Si^{4+} ions in $Mg_{0.5}Zr_2(PO_4)_3$ has been studied. Structurally, Si^{4+} ions have a smaller ionic radius than Zr^{4+} (ionic radius difference of 0.40 Å), and at 800°C, this substitution results in the highest conductivity due to the optimal lattice size it creates. Electrically, the $Mg_{0.5}Si_2(PO_4)_3$ ceramic exhibited a stable voltage window of 3.2 V at ambient temperature, demonstrating its wide and stable voltage range [10].

Several researchers have investigated the effects of Cr^{3+} ion substitution on the conductivity properties of NASICON-structured compounds, though studies remain limited, and the incorporation of Cr^{3+} into $LiSn_2P_3O_{12}$ has been shown to enhance structural and electrical properties. Structurally, it leads to increased crystallinity and homogeneity, along with changes in lattice constants. Electrically, Cr^{3+} substitution improves conductivity, reaching up to 10^{-6} $S{\cdot}cm^{-1}$, while similarly, Cr^{6+} substitution in $La_2Mo_2O_9$ has been explored [11,12]. Due to the smaller ionic radius of Cr^{6+} (0.44 Å) compared to Mo^{6+} (0.59 Å), structural modifications occur, leading to a reduction in unit cell volume and limiting free space for oxygen diffusion. As a result, overall conductivity decreases compared to $La_2Mo_2O_9$. However, at lower temperatures, samples with higher Cr content exhibit notable improvements in conductivity.

Although the solid-state method has been widely used to prepare NASICON materials, it has drawbacks, such as requiring high temperatures, potential contamination, volatilization, lack of microstructure control, and difficulties in achieving excellent ceramics without intergranular resistance. The sol-gel method, on the other hand, offers advantages, including lower reaction temperatures, improved conductivity of grain boundaries, and excellent homogeneity due to its high-purity nature [4]. Furthermore, there is limited research on the effects of Chromium substitution in $Mg_{0.5}Ti_2(PO_4)_3$ solid

electrolytes, particularly regarding their structural and electrical properties. Thus, this study aims to explore Chromium substitution in $Mg_{0.5}Ti_2(PO_4)_3$ and contribute valuable insights into magnesium-based NASICON compounds.

2. MATERIALS AND METHODS

2.1 Synthesis of $Mg_{0.5+\frac{x}{2}}Cr_xTi_{2-x}(PO_4)_3$ Samples

First, $Mg(CH_3COO)_2{\cdot}4H_2O$ and $NH_4H_2PO_4$ were dissolved in distilled water, while $C_{16}H_{36}O_4Ti$ and $C_6H_9CrO_6$ were dissolved in ethanol under magnetic stirring. The solutions of $Mg(CH_3COO)_2{\cdot}4H_2O$ and $NH_4H_2PO_4$ were then combined under continuous stirring to form a homogeneous mixture. Next, $C_{16}H_{36}O_4Ti$ and $C_6H_9CrO_6$ were gradually added to the $Mg(CH_3COO)_2{\cdot}4H_2O$ and $NH_4H_2PO_4$ solution. Once a homogeneous solution was achieved, the mixture was stirred at 70 °C for approximately 3 hours. The resulting gel was then dried in an oven at 120 °C for 24 hours to eliminate residual organic components and water. The dried precursor was ground for 30 minutes to obtain a fine powder, which was then sintered at 850 °C for 24 hours. After sintering, the final product was further ground for another 30 minutes. Finally, the fine powder was compressed using a Specac hydraulic press at 5 tonnes of pressure to form pellets with a diameter of 13 mm and a thickness ranging from 1.00 to 3.00 mm [13].

2.2 Characterizations Technique

The structural properties of the samples were analyzed using a PANalytical X'Pert³ X-ray diffractometer with Cu-Kα radiation at a wavelength of 1.5406 Å. For XRD analysis, a small amount of powdered sample was evenly spread onto a glass slide using a flat spatula and then placed in the sample holder. The sample was scanned with a step size of 0.026° over a 2θ range from 10° to 45°. For infrared spectroscopy, IR radiation was passed through the sample, with some radiation being absorbed and some transmitted. The analysis was conducted in the spectral region of 550 cm^{-1} to 1400 cm^{-1} at room temperature, producing a spectrum that represents the molecular absorption and transmission, effectively creating a molecular fingerprint of the sample. When exposed to IR radiation, the sample molecules absorbed radiation at specific wavelengths corresponding to the bonds present.

In this study, a Perkin-Elmer Frontier Spectrometer was used for sample characterization. The powdered sample was placed on an ATR crystal and analyzed at room temperature with a scan resolution of 2 cm^{-1} over a wavelength of 400 cm^{-1} to 4000 cm^{-1}. The surface morphology of the sintered samples was analyzed using Scanning Electron Microscopy (SEM) with a Zeiss Evo MA10 microscope. The electrical properties of the prepared samples were evaluated using AC impedance electrochemical spectroscopy with a Solartron 1260 Impedance/Gain Phase Analyzer, covering a wavelength of 1 Hz to 10^6 Hz. A fixed voltage of 200 mV was applied, and all measurements were conducted at room temperature.

3. RESULTS AND DISCUSSION

3.1 Structural Analysis

In the present study, an effort to enhance the ionic conductivity of $Mg_{0.5+\frac{x}{2}}Cr_xTi_{2-x}(PO_4)_3$ compound was made by substituting Ti^{4+} site using a smaller trivalent ion in Cr^{3+} (r_{ion} = 0.615 Å) with the goal of creating Mg initial ion. X-ray diffraction analysis is used to study the structural properties of $Mg_{0.5+\frac{x}{2}}Cr_xTi_{2-x}(PO_4)_3$. Figure 1 shows the XRD analysis patterns of $Mg_{0.5+\frac{x}{2}}Cr_xTi_{2-x}(PO_4)_3$ samples with different values of x, ranging from 0.1, 0.3, 0.5, 0.7, and 0.9.

From Figure 1, the X-ray diffraction patterns of the samples reveal that all samples exhibit well-defined diffraction peaks, confirming the formation of a crystalline NASICON-type phase. The major reflections can be indexed to a hexagonal rhombohedral structure with space group R3c, consistent with the reported structure of $MgTi_2(PO_4)_3$. It is also known that $Mg_{0.5}Ti_2(PO_4)_3$ may crystallize in either the R3 or R3c space group, depending on synthesis temperature and cation distribution [13].

Distinct peaks are observed at 2θ ≈ 21°, 25°, 30°, 33°, and 37°, corresponding to the characteristic planes of the NASICON framework. However, minor impurity peaks appear near 20° and 25°, particularly in the samples with lower Cr content. These peaks are most likely associated with residual TiO_2 (anatase phase) or magnesium pyrophosphate ($Mg_2P_2O_7$), which can form due to incomplete decomposition of precursors or insufficient phosphate diffusion during the sol–gel combustion stage. The presence of such weak reflections suggests localized inhomogeneities or incomplete crystallization that are common in sol–gel–derived powders when the calcination duration is limited.

As the Cr content increases ($x = 0.1 \rightarrow 0.9$), the intensity of these impurity peaks gradually decreases, implying that Cr substitution promotes better phase homogeneity and crystallization by enhancing cationic diffusion and lattice stabilization. Nevertheless, traces of secondary phases remain, indicating that a slightly higher sintering temperature or prolonged heat treatment could further improve phase purity and eliminate the residual precursors [10].

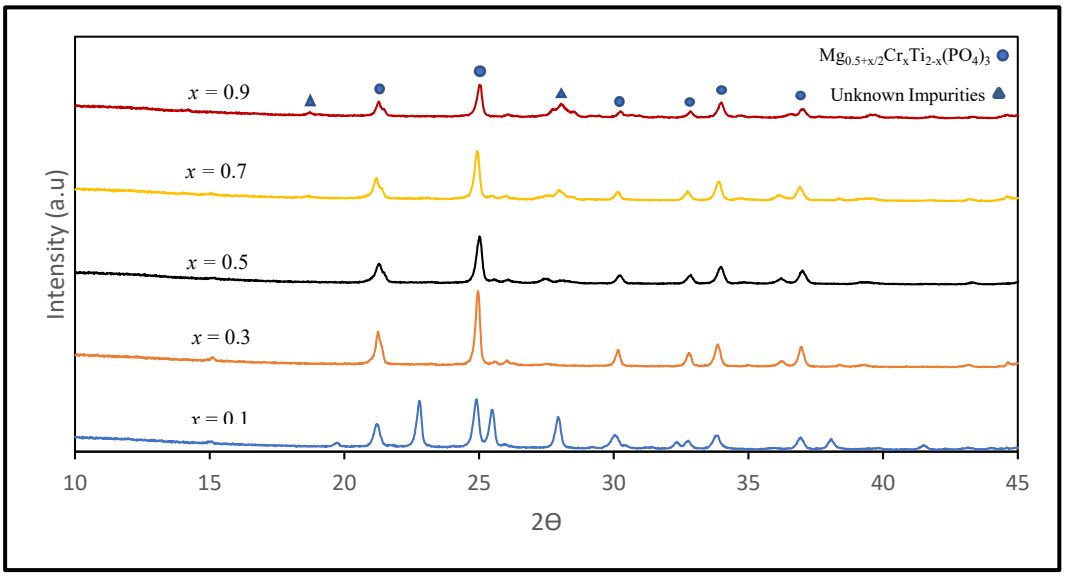

Figure 1: X-ray diffraction patterns of $Mg_{0.5+\frac{x}{2}}Cr_xTi_{2-x}(PO_4)_3$ system

FTIR has been employed to identify the functional group in $Mg_{0.5+\frac{x}{2}}Cr_xTi_{2-x}(PO_4)_3$ system. Figure 2 shows the FTIR spectra of various functional groups of the samples, respectively, in the spectral region of 550 to 1300 cm^{-1}. The absorption bands observed in the 550 cm^{-1} to 680 cm^{-1} region correspond to the asymmetric bending vibration modes of O-P-O units [8]. These bands, as seen in the FTIR spectrum, are characteristic of the structural vibrations associated with phosphate groups. Meanwhile, the bands in the 680 cm^{-1} to 870 cm^{-1} range can be attributed to the stretching vibrations of P-O-P units, further confirming the presence of phosphate frameworks within the material.

In addition, the spectral region between 870 cm^{-1} and 1000 cm^{-1} exhibits asymmetric stretching vibrations, which indicate the dynamic bonding behaviour of the phosphate tetrahedral units. Moving to the 1000 cm^{-1} to 1300 cm^{-1} range, symmetric stretching vibrations are observed, signifying the presence of stable phosphate linkages. Across the entire spectral region, the dominant feature is the vibration of the PO_4 tetrahedral structure, which plays a crucial role in defining the material's overall

structural integrity. Furthermore, the substitution of Li^{+} with Mg^{2+} in the NASICON structure does not introduce noticeable distortions, suggesting that the anion ring remains stable even after the ionic substitution. This stability is a key factor in preserving the structural framework, ensuring the material retains its functional properties [3].

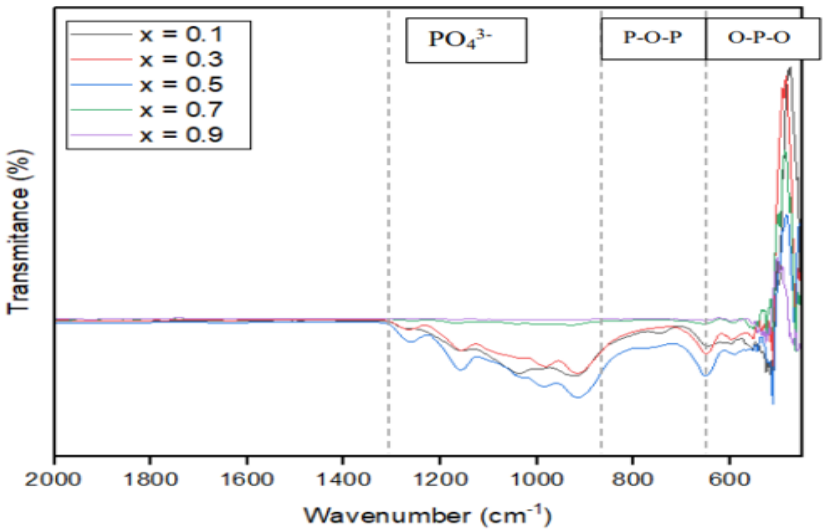

Figure 2: FTIR spectra of various functional groups in $Mg_{0.5+\frac{x}{2}}Cr_xTi_{2-x}(PO_4)_3$ system

3.2 Morphological Analysis

Figure 3 shows SEM images of $Mg_{0.5+\frac{x}{2}}Cr_xTi_{2-x}(PO_4)_3$ taken at a magnification of 2500×. The microstructural analysis through SEM reveals that the material exhibits a heterogeneous grain structure, characterized by grains of varying sizes. Some grains appear larger and well-defined, as shown in Figure 3(a) and (b), while others are significantly smaller and more dispersed throughout the matrix, as shown in Figure 3(c) to (e). Generally, larger grains may lead to increased brittleness, whereas a combination with smaller grains can enhance the overall toughness and durability.

Table 1 shows the grain size statistics from the SEM analysis. The grain-size analysis of the sintered samples x = 0.1 to 0.9 derived from SEM micrographs at 2,500× magnification (30 µm scale bar) revealed a progressive refinement of the microstructure. The samples with x = 0.1 exhibited the largest and most heterogeneous grains (mean ≈ 16.5 µm), indicative of coarse-grain growth during high-temperature sintering. Sample with x showed a noticeable reduction in mean grain size (≈ 10.7 µm), suggesting partial suppression of abnormal grain growth.

A significant transition occurred in x = 0.5, 0.7 and 0.9, where the mean grain sizes decreased to ≈ 3.1, 2.8, and 2.8 µm, respectively, with narrower distributions reflecting a more homogeneous and fine-grained microstructure. Furthermore, the SEM images indicate that as the x value increases, the introduction of Chromium ions influences the crystallization process by promoting nucleation while simultaneously inhibiting excessive grain growth. This interaction results in a progressive reduction in particle size, contributing to a refined microstructure in the NASICON-type material.

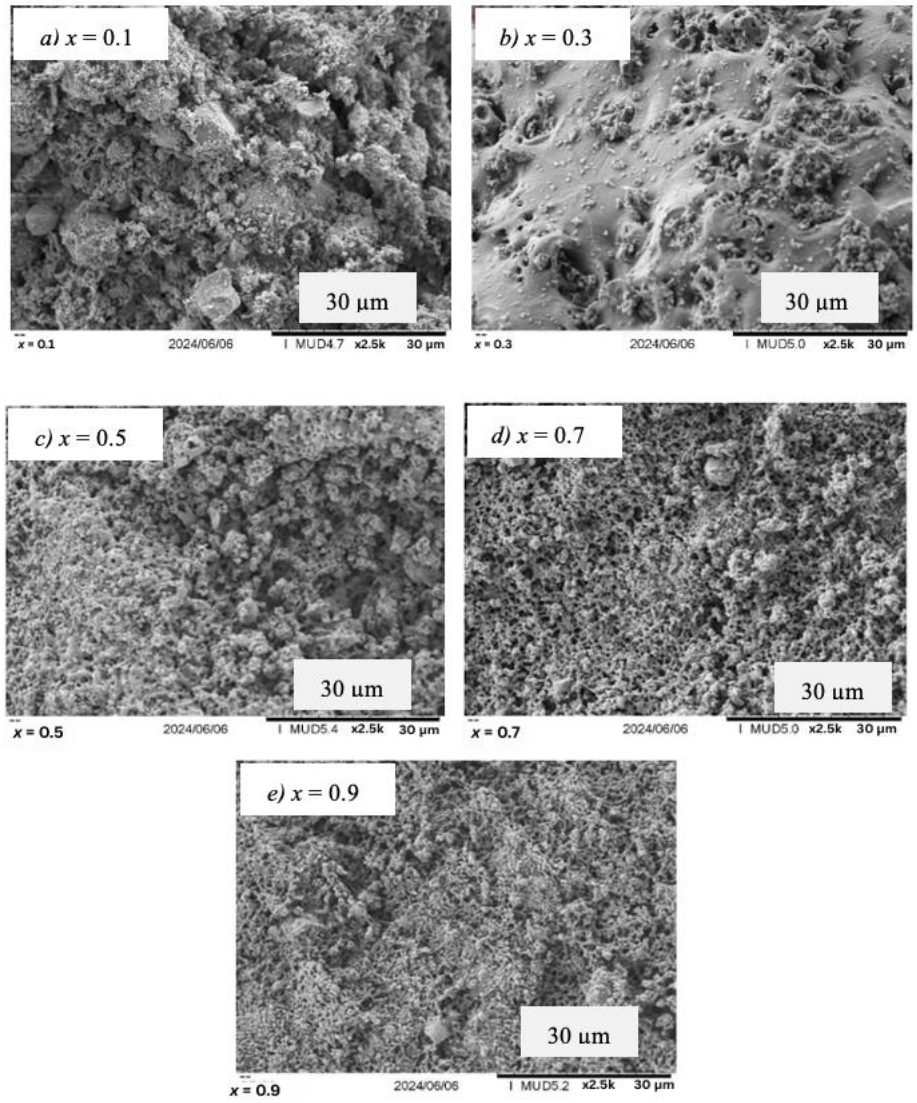

Figure 3: SEM images of $Mg_{0.5+\frac{x}{2}}Cr_xTi_{2-x}(PO_4)_3$, (a) $x = 0.1$, (b) $x = 0.3$, (c) $x = 0.5$, (d) $x = 0.7$ and (e) $x = 0.9$

Table 1: Grain size statistics of $Mg_{0.5+\frac{x}{2}}Cr_xTi_{2-x}(PO_4)_3$ samples

Sample (Value of x)	Mean Grain Size (µm)	Median Grain Size (µm)	Standard Deviation (µm)
0.1	16.54	15.13	± 9.55
0.3	10.65	9.82	± 4.87
0.5	3.10	2.44	± 1.82
0.7	2.83	2.32	± 1.67
0.9	2.78	2.28	± 1.78

3.3 Electrical Analysis

Electrochemical Impedance Spectroscopy (EIS) analysis was performed to investigate the electrical properties of $Mg_{0.5+\frac{x}{2}}Cr_xTi_{2-x}(PO_4)_3$ samples under room temperature conditions. This technique is widely used to analyze the resistive and capacitive behavior of materials, providing

valuable insights into their conduction mechanisms. The impedance data obtained from the analysis help in understanding the charge transport properties and overall electrical behavior of the synthesized materials. Figure 4 displays the impedance plots for the $Mg_{0.5+\frac{x}{2}}Cr_xTi_{2-x}(PO_4)_3$ samples, with x = 0.1, 0.3, 0.5, 0.7, and 0.9.

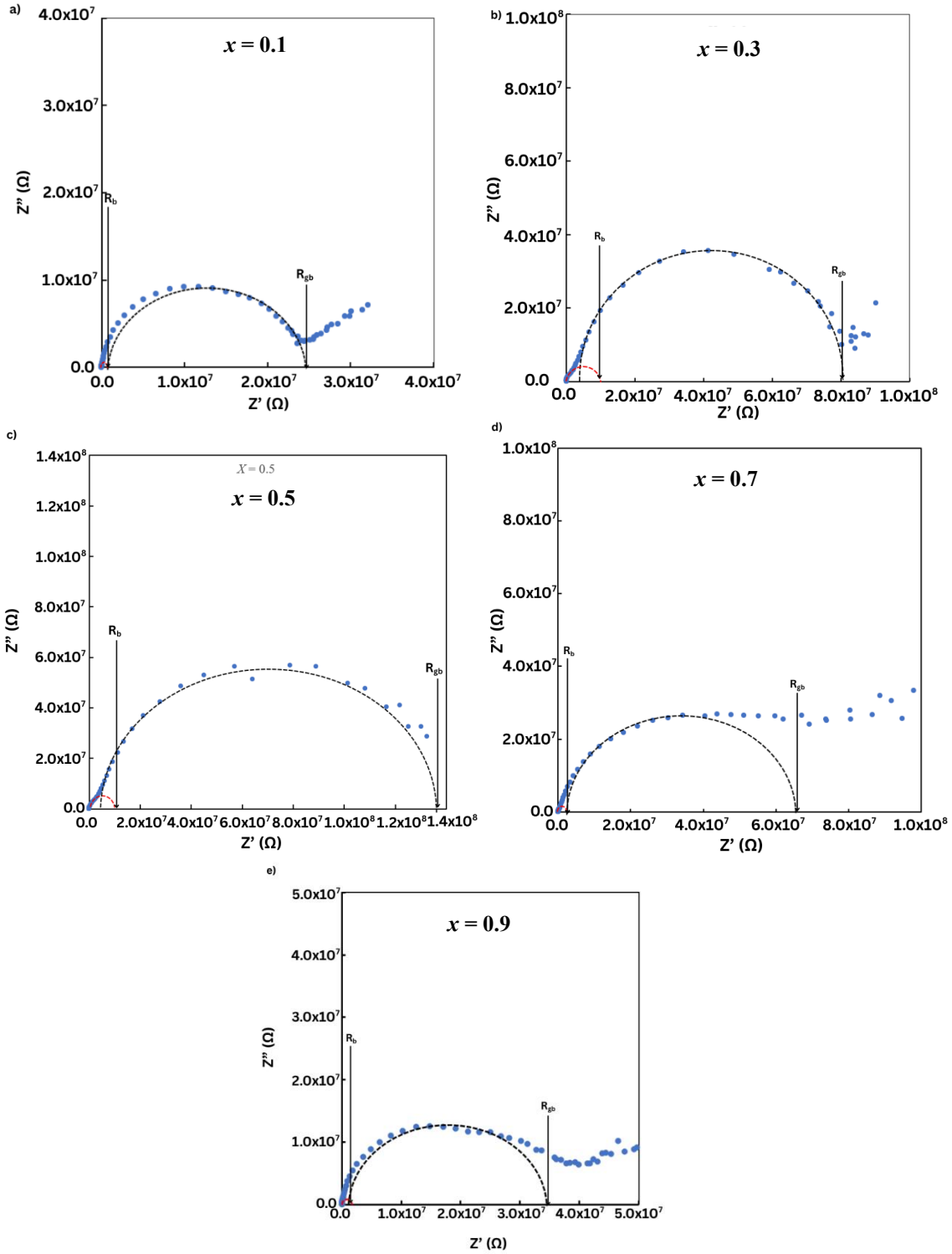

Figure 4: Impedance plot of $Mg_{0.5+\frac{x}{2}}Cr_xTi_{2-x}(PO_4)_3$ (a) x = 0.1, (b) x = 0.3, (c) x = 0.5, (d) x = 0.7 and (e) x = 0.9

These impedance plots are crucial in determining the resistance contributions from different components of the material, particularly the bulk and grain boundary resistances. In the impedance plots, both resistances are represented by semicircles, which provide information regarding the conductive nature of the sample. The impedance spectra exhibit two distinct compressed semicircles at the x-axis intercept, corresponding to the bulk resistance (R_b) and the grain boundary resistance (R_{gb}). The smaller compressed semicircle appearing at lower x-axis values represents the bulk resistance (R_b), which is associated with the intrinsic resistance of the material's grains. Meanwhile, the larger compressed semicircle appearing at higher x-axis values corresponds to the grain boundary resistance (R_{gb}), which arises due to the interfacial resistance between the grains. These resistance values play a significant role in determining the overall conductivity of the material, influencing its potential applications in electrochemical devices.

As the Cr content increases from x = 0.1 to 0.5, where it can be observed in Figure 4(a) to (c), the semicircle corresponding to bulk resistance (R_b) expands, which can be attributed to a decline in conductivity. This suggests that the material's intrinsic resistance increases within this range, leading to reduced charge transport efficiency. However, as the x value further increases from 0.5 to 0.9, as shown in Figure 4(d) and (e), conductivity improves in the high-frequency region, resulting in a noticeable reduction in the size of the bulk resistance semicircle. This indicates a lower intrinsic resistance, facilitating better charge transport within the material.

A similar pattern is observed for the semicircle representing grain boundary resistance (R_{gb}) in the middle-frequency region. As the x value increases from 0.1 to 0.5, the semicircle expands, suggesting that the resistance at the grain boundaries increases due to decreased conductivity. However, as the x value continues to rise from 0.5 to 0.9, the grain boundary resistance semicircle contracts, reflecting an enhancement in conductivity and improved charge mobility across the grain interfaces. These changes in resistance behaviour highlight the influence of Cr compositional variations on the electrical properties of the material.

Meanwhile, the overlapped semicircles as observed in Figure 4, the impedance spectrum can be observed in the equivalent circuit of the impedance plot of $Mg_{0.5+\frac{x}{2}}Cr_xTi_{2-x}(PO_4)_3$ sample is displayed in Figure 5. This circuit consists of parallel RC elements in series with constant phase elements (CPE). CPE stands for circuit arrangement in which series with bulk resistance and grain boundary resistance, whereas both are parallel to the capacitor.

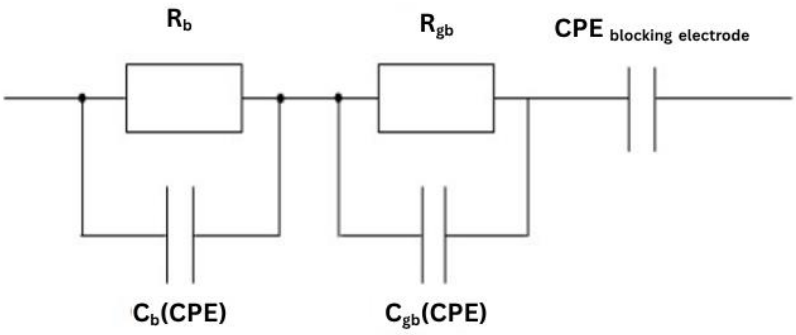

Figure 5: Equivalent circuit of $Mg_{0.5+\frac{x}{2}}Cr_xTi_{2-x}(PO_4)_3$ samples based on the impedance analysis of the samples at room temperature

The data from Table 2 indicate that bulk conductivity varies with x. As x increases from 0.1 to 0.5, bulk conductivity decreases from 8.68×10^{-8} S.cm^{-1} to 1.36×10^{-8} S.cm^{-1}. This decline is attributed

to lattice strain-induced narrowing of conduction channels and increased migration barriers [12]. However, as x further increases from 0.5 to 0.9, bulk conductivity rises from 1.36×10^{-8} S.cm^{-1} to 8.97×10^{-8} S.cm^{-1}. This enhancement in conductivity is likely due to the increased polarizability of Cr ions and possible disorder in the occupancy of vacant sites, facilitating charge transport 11].

As seen from Table 2, the grain boundary conductivity varies with the x value. As x increases from 0.1 to 0.5, grain boundary conductivity decreases from 4.66×10^{-9} S.cm^{-1} to 9.58×10^{-10} S.cm^{-1}. However, as x further increases from 0.5 to 0.9, grain boundary conductivity rises from 9.58×10^{-10} S.cm^{-1} to 3.95×10^{-9} S.cm^{-1}. This variation is attributed to structural changes within the samples, which influence grain boundary conductivity [1]. The improvement in conductivity can also be linked to better grain-to-grain contact, resulting from increased homogeneity within the material [11]. Plus, data from Table 2 clearly demonstrate that the total conductivity varies depending on the x values. Specifically, as the x value increases from 0.1 to 0.5, there is a noticeable decrease in total conductivity, dropping from 4.42×10^{-9} S.cm^{-1} to 8.96×10^{-10} Scm^{-1}. This reduction suggests a decrease in the material's charge transport efficiency as the Cr content rises. However, when the x value increases further from 0.5 to 0.9, the total conductivity begins to increase once more, reaching a value of 3.78×10^{-9} S.cm^{-1}. This trend indicates a recovery or improvement in conductivity with higher Cr content beyond $x = 0.5$, showing an increase in charge transport efficiency as Cr content is higher in the samples.

Table 2: Bulk, grain boundary, and total conductivity of $Mg_{0.5+\frac{x}{2}}Cr_xTi_{2-x}(PO_4)_3$ samples

Sample (Value of x)	Bulk conductivity, σ_b (S.cm^{-1})	Grain boundary conductivity, σ_{gb} (S.cm^{-1})	Total conductivity, σ_t (S.cm^{-1})
0.1	8.68×10^{-8}	4.66×10^{-9}	4.42×10^{-9}
0.3	1.41×10^{-8}	1.52×10^{-9}	1.37×10^{-9}
0.5	1.36×10^{-8}	9.58×10^{-10}	8.96×10^{-10}
0.7	6.85×10^{-8}	1.89×10^{-9}	1.84×10^{-9}
0.9	8.97×10^{-8}	3.95×10^{-9}	3.78×10^{-9}

All values of bulk conductivity, grain boundary conductivity and total conductivity of value of x is shown in Table 2. The total conductivity peaks at $x = 0.1$, suggesting that a small amount of Cr^{3+} substitution optimally enhances charge transport. This enhancement is attributed to heterovalent $Ti^{4+} \rightarrow Cr^{3+}$ substitution, which generates charge-compensating oxygen vacancies that improve carrier concentration while maintaining the integrity of the NASICON-type framework. A further increase in Cr content ($x \geq 0.3$) suppresses bulk conductivity at $x = 0.5$, accompanied by a reduction in total conductivity, which is consistent with lattice strain-induced narrowing of conduction channels and increased migration barriers [11]. The SEM analysis corroborates this trend, revealing a progressive grain refinement from ≈ 16.5 µm at $x = 0.1$ to ≈ 3 µm at higher Cr levels, which increases grain-boundary resistance and accounts for the reduced values.

At higher substitution levels ($x > 0.5$), however, a partial recovery of conductivity is observed, which can be attributed to increased lattice polarizability of Cr ions and disorder in the vacancy sub-lattice that collectively facilitate carrier hopping. This recovery is further supported by improved grain-to-grain contact and enhanced microstructural homogeneity, leading to better grain-boundary conductivity [1,11]. These results indicate that $x = 0.1$ represents the optimal Cr substitution level, achieving the highest conductivity by balancing defect generation and structural stability. Overall, the conductivity trend reflects the interplay between vacancy-driven carrier generation at low x, lattice-strain-limited transport at intermediate x, and polarizability-assisted hopping at high x, highlighting the crucial role of Cr substitution in tuning the electrical performance of $Mg_{0.5+\frac{x}{2}}Cr_xTi_{2-x}(PO_4)_3$ samples.

As the interest in Mg^{2+} ion electrolytes increases among researchers, there are a lot of studies in understanding the structural and electrical properties of Mg^{2+} ion NASICON electrolytes. These are some previous studies on Mg^{2+} ion NASICON electrolytes, shown in Table 3.

Table 3: Previous research on Mg^{2+} ion NASICON electrolytes

Research	Conductivity Value	Temperature	Reference
Cr^{3+} substitution in $Mg_{0.5}Ti_2(PO_4)_3$	4.42×10^{-9} S.cm^{-1}	RT	This work
$Mg_{0.5}Zr_2(PO_4)_3$ NASICON	1.0×10^{-6} S.cm^{-1}	RT	[3]
Fe^{3+} substitution (y = 0.4) in $Mg_{0.5+\gamma}(Zr_{1-\gamma}Fe_\gamma)_2(PO_4)_3$	1.25×10^{-5} S.cm^{-1}	RT	[4]
	7.18×10^{-5} S.cm^{-1}	773 K	
$Mg_{0.5}Ti_2(PO_4)_3$ (sintered)	σ_b: 1.7×10^{-3} S.cm^{-1}	600 °C	[9]
	σ_{gb}: 1.9×10^{-5} S.cm^{-1}	600 °C	
$MgZr_4(PO_4)_6$	2.9×10^{-5} S.cm^{-1}	400 °C	[14]
	6.1×10^{-3} S.cm^{-1}	800 °C	
Si^{4+} for P^{5+} in $MgZr_4(PO_4)_6$	1.4×10^{-5} S.cm^{-1}	(Not stated, likely RT)	[15]
Sn^{4+} substitution in $Mg_{0.5}Zr_2(PO_4)_3$	3.54×10^{-7} S.cm^{-1} → 2.47×10^{-5} S.cm^{-1}	500 °C	[16]
$Mg_{0.5}Ti_2(PO_4)_3$ (high T)	2.63×10^{-7} S.cm^{-1}	500 °C	[17]
Ce-doped $MgZr_4(PO_4)_6$	1.063×10^{-8} S.cm^{-1}→ 1.16×10^{-7} S.cm^{-1}	(Not stated)	[18]
$Mg_{0.6}Fe_{0.2}Zr_{1.8}(PO_4)_3$ film	Resistance: 1.6 kΩ·cm²	200 °C	[19]
$(Mg_xHf_{1-x})_{4/4-2x}Nb(PO_4)_3$ (x = 0.1)	Higher c-axis conductivity & negative thermal expansion	(Not specified)	[20]

4. CONCLUSIONS

The NASICON-structured material $Mg_{0.5+\frac{x}{2}}Cr_xTi_{2-x}(PO_4)_3$ was successfully synthesized using the sol-gel method with x values of 0.1, 0.3, 0.5, 0.7, and 0.9 to reduce impurities. XRD analysis showed a hexagonal structure with the R3c space group and some unidentified impurities, with the x = 0.1 sample exhibiting the highest crystallinity and conductivity. FTIR results indicated that PO_4 tetrahedral vibrations dominated across all samples. SEM analysis showing that increasing the Cr content from 0.1 to 0.9 progressively refines the grain structure, resulting in smaller and more homogeneous grains. EIS analysis revealed that the highest bulk conductivity was at x = 0.9 (8.97×10^{-8} S.cm^{-1}), while the highest grain boundary conductivity was at x = 0.1 (4.66×10^{-9} S.cm^{-1}). Overall, the highest total conductivity was at x = 0.1 (4.42×10^{-9} S.cm^{-1}). In conclusion, Cr substitution significantly influences the structural and electrical properties of Mg-based solid electrolytes. The research has great potential for the future of magnesium-based solid electrolyte development, with further studies needed to be conducted and applied in innovations.

Acknowledgements

The authors sincerely acknowledged both Universiti Teknologi MARA (UiTM) and International Battery Centre (IBC) for all the help and support in finishing the work in order to successfully complete the research.

Author Contributions

All authors contributed toward data analysis, drafting, and critically revising the paper and agree to be accountable for all aspects of the work.

Disclosure of Conflict of Interest

The authors have no disclosures to declare.

Compliance with Ethical Standards

The work is compliant with ethical standards.

References

[1] Takahashia, H. & Takamura, H. (2012). Ionic conductivity and crystal structure of tm doped $Mg_{0.5}Ti_2(PO_4)_3$ (TM = Fe, Mn, Co and Nb). *Key Engineering Materials*, 508, 291-299.

[2] Saha, P., Datta, M. K., Velikokhatnyi, O. I., Manivannan, A., Alman, D. & Kumta, P. N. (2014). Rechargeable magnesium battery: current status and key challenges for the future. *Progress in Materials Science*, 66, 1-86.

[3] Anuar, N. K., Adnan, S. B. R. S. & Mohamed, N. S. (2014). Characterization of $Mg_{0.5}Zr_2(PO_4)_3$ for potential use as electrolyte in solid state magnesium batteries. *Ceramics International,* 40(8), 13719–13727.

[4] Anuar, N. K., Adnan, S. B. R. S., Jaafar, M. H. & Mohamed, N. S. (2016). Studies on structural and electrical properties of $Mg_{0.5+y}(Zr_{2-y}Fe_y)_2(PO_4)_3$ ceramic electrolytes. *Ionics,* 22(7), 1125–1133.

[5] Besenhard, J. O. & Winter, M. (2002). Advances in battery technology: rechargeable magnesium batteries and novel negative-electrode materials for lithium-ion batteries. *ChemPhysChem,* 3(2), 155–159.

[6] Aurbach, D., Zinigrad, E., Cohen, Y. & Teller, H. (2002). A short review of failure mechanisms of lithium metal and lithiated graphite anodes in liquid electrolyte solutions. *Solid State Ion*, 148(3-4), 405–416.

[7] Dzulkurnain, N. A., Mustaffa, N. A. & Mohamed, N. S. (2017). Structural, Electrical and Electrochemical Properties of $Mg_{0.55}Si_{1.9}Al_{0.1}Fe_{0.1}(PO_4)_3$ Ceramic Electrolytes. *Journal of New Materials for Electrochemical Systems*, 20, 135-140.

[8] Mustaffa, N. A., Adnan, S. B. R. S., Sulaiman, M. & Mohamed, N. S. (2015). Low-temperature sintering effects on NASICON-structured $LiSn_2P_3O_{12}$ solid electrolytes prepared via citric acid-assisted sol-gel method. *Ionics,* 21(4), 955–965.

[9] Makino, K., Katayama, Y., Miura, T. & Kishi, T. (2001). Electrochemical insertion of magnesium to $Mg_{0.5}Ti_2(PO_4)_3$. *Journal of Power Sources*. 99(1-2), 66-69.

[10] Halim, Z. A., Adnan, S. B. R. S. & Mohamed, N. S. (2016). Effect of sintering temperature on the structural, electrical and electrochemical properties of novel $Mg_{0.5}Si_2(PO_4)_3$ ceramic electrolytes. *Ceramics International,* 42(3), 4452–4461.

[11] Norhaniza, R., Subban, R. H. Y., Mohamed, N. S. & Ahmad, A. (2012). Chromium substituted $LiSn_2P_3O_{12}$ solid electrolyte. *International Journal of Electrochemical Science,* 7(10), 10254-10265.

[12] Marrero-López, D., Peña-Martínez, J., Ruiz-Morales, J. C., Pérez-Coll, D., Martín-Sedeño, M. C. & Núñez, P. (2008). Cerámica y Vidrio Structural and electrical characterisation of Nb^{5+} and Cr^{6+} substituted $La_2Mo_2O_9$. *Boletín de la Sociedad Española de Cerámica y Vidrio*, 47(4), 213-218.

[13] Essehli, R., Bali, B. E. S., Benmokhtar, Fejfarová, K. & Dusek, M. (2009). Hydrothermal synthesis, structural and physico-chemical characterizations of two Nasicon phosphates: $Mg_{0.5}0_{II}Ti_2(PO_4)_3$ (M=Mn, Co). *Materials Research Bulletin*, 44(7), 1502 – 1510.

[14] Ikeda, S., Takahashi, M., Ishikawa, J. & Ito, K. (1987). Solid electrolytes with multivalent cation conduction. 1. Conducting species in $MgZr_4(PO_4)_6$ system. *Solid State Ionics*, 23(1-2), 125 -129.

[15] Nomura, K., Ikeda, S., Ito, K. & Einaga, H. (1992). Framework structure, phase transition and ionic conductivity of $MgZr_4(PO_4)_6$ and $ZnZr_4(PO_4)_6$. *Journal of Electroanalytical Chemistry*, 326(1-2), 351–356.

[16] Mustafa, M., Rani, M. S. A., Adnan, S. B. R. S., Salleh, F. M. & Mohamed, N. S. (2020). Characteristics of new $Mg_{0.5}(Zr_{1-x}Sn_x)_2(PO_4)_3$ NASICON structured compound as solid electrolytes. *Ceramics International*, 46(18), 28145–28155.

[17] Wahab, N. A., Kamil, S. A., Adnan, S. B. R. S., Dzulkurnain, N. A. & Mustaffa, N. A. (2025). Magnesium titanium phosphate ceramic electrolytes: structural, electrical and electrochemical properties. *Journal of Sol-Gel Science and Technology*, 114(1), 274 – 286.

[18] Li, M., Li, X., Gong, W., Chen, P. & Zhu, B. (2020). Tunability study on microstructure and electromagnetic properties of Ce-Doped $MgZr_4P_6O_{24}$. *Journal of Alloys and Compounds*, 820, 153097.

[19] Liu, S., Zhou, C., Wang, Y., Yi, E., Wang, W., Kieffer, J. & Laine, R. (2020). Processing combustion synthesized $Mg_{0.5}Zr_2(PO_4)_3$ nanopowders to thin films as potential solid electrolytes. *Electrochemistry Communications*, 116, 106753.

[20] Özbilgin, C., Kobayashi, K., Tamura, S., Imanaka, N. & Suzuki, T. (2022). Anisotropic thermal expansion and ionic conductivity of a crystal-oriented, Mg^{2+}-conducting NASICON-type solid electrolyte. *Ceramics International*, 48(8), 10733-10740.